Journal of Materials Chemistry A

ROYAL SOCIETY OF CHEMISTRY

PAPER

View Article Online
View Journal

Cite this: DOI: 10.1039/d6ta02888h

Interfacial electron transfer-driven activity enhancements of carbide/alloy heterostructured catalysts toward water electrolysis for high-performance anion exchange membrane water electrolysis

Kai-An Lee, Yu-Chieh Ting, Chiung-Wen Chang, Tzu-Hsiang Lin, Shao-I. Chang, Tsung-Wei Hsueh, Chia-Hsien Lin and Shih-Yuan Lu *

Designing highly efficient and durable electrocatalysts remains a key challenge for practical alkaline water electrolysis. Here, rationally designed carbide/alloy heterostructured catalysts, Mo_2C/NiMo for the hydrogen evolution reaction (HER) and Mo_2C/FeNiMo for the oxygen evolution reaction (OER), were developed for activity enhancement driven by interfacial electron transfer to enable anion exchange membrane water electrolysis (AEMWE) with extraordinary performances. Mo_2C/NiMo and Mo_2C/FeNiMo achieved ultralow overpotentials of 169 and 303 mV, respectively at 500 mA cm^{-2}. The Mo_2C//NiMo@NF//PiperION//Mo_2C//FeNiMo@NF based AEMWE delivered an exceptionally high current density of 2.645 A cm^{-2} at 2.0 V, along with an insignificant 2.0% decay after 50 h of operation at a commercially relevant current density of 0.5 A cm^{-2}, underscoring its outstanding catalytic efficiency and durability. In the two carbide/alloy heterostructured catalysts, electrons flow from the alloy domain to the carbide domain, triggering interfacial synergy. The interfacial synergy promotes efficient coupling of water dissociation and H_2 desorption along the Volmer–Heyrovsky route to boost the HER activities of Mo_2C/NiMo, and creates more electropositive Fe and Ni sites for favorable formation of active high-valent intermediates to realize high OER activities of Mo_2C/FeNiMo. This work highlights the great promise of carbide/alloy heterostructures as advanced electrocatalysts for scalable and efficient alkaline water electrolysis.

Received 6th April 2026
Accepted 12th May 2026

DOI: 10.1039/d6ta02888h

rsc.li/materials-a

1. Introduction

With the rise in global environmental awareness, achieving net-zero carbon emissions has become a core objective in global energy development. And the development of clean energy alternatives to fossil fuels has become a critical issue.[1] Hydrogen has emerged as a key enabler of the on-going energy transition because of its high energy density and carbon-free nature. Beyond serving as a clean fuel, hydrogen also plays a critical role in power generation and industrial energy supply, and as a high-value chemical feedstock.[2] Therefore, the development of sustainable and scalable hydrogen production technologies is of paramount importance for advancing green energy infrastructure. In this regard, electrocatalytic water splitting stands out as a promising green hydrogen production technology,[3] and in particular anion exchange membrane water electrolysis (AEMWE) emerges as a favorable water-splitting technology.[4,5]

AEMWE integrates the advantages of both proton exchange membrane water electrolysis (PEMWE) and alkaline water electrolysis (AWE), enabling the use of non-precious transition metal catalysts for cost-effective, efficient, and stable water electrolysis operations.[6,7] Membrane electrode assembly (MEA), the core working unit of an AEMWE, is composed of two catalyst loaded electrodes, the cathode and anode, and an anion exchange membrane (AEM).[8] The catalysts loaded at the cathode and anode catalyze the hydrogen evolution reaction (HER) and oxygen evolution reaction (OER), respectively, playing a decisive role in governing the overall efficiency of an AEMWE. Rational design of electrocatalysts specifically tailored for the two fundamental reactions of water electrolysis, HER and OER, in alkaline media is thus critical for the prevalence of the AEMWE technology for green hydrogen production.

A wide variety of strategies for advancing catalyst performances have been proposed and explored, including nanostructure control, defect engineering, heteroatom doping, alloying, construction of heterostructures, *etc.* Heterostructured materials, in particular, have drawn increasing attention in recent years as promising electrocatalysts for a wide range of

Department of Chemical Engineering, National Tsing Hua University, Hsinchu 300044, Taiwan. E-mail: sylu@mx.nthu.edu.tw

electrochemical reactions, including HER, OER, oxygen reduction reaction, *etc.*[9,10] A heterostructure is generally defined as a composite material composed of two or more distinct solid-state phases that form well-defined heterointerfaces. Compared with their single-phase counterparts, heterostructured catalysts typically exhibit superior catalytic activities, which can be attributed to several advantages. First, the creation of heterostructures can substantially increase the density of accessible active sites. In addition, rationally designed nanostructured morphologies within heterostructures can further enhance structural robustness and durability during electrochemical operations.[11] In addition, the electronegativity difference between distinct components within a heterostructure often drives electron transfer across the interface. This interfacial electron redistribution can modulate the local electronic structure or even the overall band structure, thereby optimizing the adsorption energies of key intermediates and ultimately enhancing the catalytic activity.[12] Finally, the synergistic effect plays a pivotal role in the design of heterostructured catalysts. By integrating complementary functionalities at the heterointerface, such effects not only introduce additional active sites for adsorption/desorption but also optimize the reaction pathways, thereby markedly enhancing the overall catalytic performance.[13]

Transition metal carbides (TMCs) have garnered significant attention as promising electrocatalysts because of their unique electronic structures, high electrical conductivities, and noble-metal-like catalytic properties.[14] The strong orbital hybridization between transition metals and carbon atoms can induce a downshift of the d-band center, thereby optimizing the metal–hydrogen binding energy. Such optimization promotes more favorable hydrogen adsorption–desorption kinetics, ultimately enhancing the catalytic performance toward HER.[15,16] Furthermore, metal carbides can also function as an integral component of heterostructured materials, thereby imparting outstanding catalytic activities. For instance, Diao *et al.* employed a simple solid-state synthesis strategy to construct W_2N/WC heterostructured catalysts. Benefiting from the abundant heterointerfaces, W_2N/WC exhibited excellent electrocatalytic performances.[17] Zhao *et al.* reported a synergistic integration of Mo_2C and MoS_2, forming a hybrid nanostructure of vertically aligned MoS_2/Mo_2C nanosheets. In this architecture, the edges of the two-dimensional MoS_2 provided a favorable environment for the uniform dispersion of Mo_2C, thereby maximizing the exposure of active sites and consequently enhancing the overall catalytic performance.[18] Xu *et al.* manipulated the Mo–H binding energy by incorporating transition metals (Ni, Co, or Fe) into Mo_2C. This modulation originates from the interfacial interactions between the transition metals and Mo_2C.[19] In addition to assessing catalytic activities through electrochemical performance measurements, further insights into the intrinsic properties of the catalysts can be obtained by density functional theory (DFT) calculations. Yuan *et al.* designed an electrode composed of Mo–Mo_2C on a Mo plate, and DFT results revealed that the incorporation of metallic Mo into the heterostructure optimizes the electronic structure of Mo_2C. This modification not only lowers the energy barrier for water dissociation but also tunes the hydrogen adsorption free energy, thereby contributing to the enhanced catalytic performance.[20]

Based on the aforementioned studies, it is evident that transition metals can interact with metal carbides to enhance catalytic activities through the formation of heterointerfaces and interfacial electron transfer. Building on this insight, we developed two distinct heterostructured electrocatalysts tailored for HER and OER, respectively. These catalysts, composed of Mo_2C and transition metal alloys, leverage the synergy between the metal carbide and alloy phases to achieve superior water splitting performances. In this work, a simple and fast dip–roast-reduction process was developed to uniformly load carbide/alloy heterostructured catalysts onto nickel foam (NF) substrates. In terms of material design, Mo_2C/NiMo was prepared for HER, whereas Mo_2C/FeNiMo was designed for OER. For HER, Mo_2C/NiMo required overpotentials of only 37 and 169 mV to reach current densities of 10 and 500 mA cm^{-2}, respectively whereas Mo_2C/FeNiMo delivered the same current densities at overpotentials of only 218 and 303 mV, respectively. When integrated as the cathode and anode in an AEMWE, these catalysts enabled a remarkably high current density of 2.645 A cm^{-2} at 2.0 V, demonstrating exceptional catalytic efficiency. Furthermore, *in situ* X-ray absorption spectroscopy (XAS) and *in situ* Raman spectroscopy were conducted to probe the reaction mechanisms, offering mechanistic insights into the origin of the enhanced activity. Overall, the rational design of carbide/alloy heterostructured catalysts presented here demonstrates significant potentials for commercial scale AEMWE, providing a promising pathway toward sustainable green hydrogen production to help reach the net-zero carbon emission goal.

2. Experimental section

2.1. Chemicals

Iron(II) chloride tetrahydrate ($FeCl_2 \cdot 4H_2O$, 98.0%), platinum (20 wt% on carbon black), and iridium(IV) oxide (IrO_2, >99.99%) were purchased from Thermo Fisher Scientific. Molybdenum(V) chloride ($MoCl_5$, >99.6%) and Nafion D-521 dispersion (5% w/w in water and 1-propanol) were purchased from Alfa Aesar. Nickel(II) chloride hexahydrate ($NiCl_2 \cdot 6H_2O$, 96.0%) was obtained from Showa Chemical Industry Co., Ltd. Carboxylic acid-modified carbon nanotubes (MCNT, AMC-C tube-010, >98.0%) were provided by Golden Innovation Business Co., Ltd. Anhydrous ethanol (99.5%) was obtained from Echo Chemical Co., Ltd. Potassium hydroxide (KOH, 85%) was purchased from Honeywell Research Chemicals. Nickel foam substrates (NF, 90 PPI with 1.7 mm in thickness and 95 PPI with 0.3 mm in thickness) were obtained from May Chun Co., Ltd. An anion exchange membrane (Versogen PiperION, 40 μm) was supplied by Fuel Cell Store.

2.2. Fabrication of Mo_2C/NiMo, Mo_2C/FeNiMo, Mo_2C, NiMo, and FeNiMo

$NiCl_2 \cdot 6H_2O$ (68.7 mM) and $MoCl_5$ (68.7 mM) were dissolved, together with 10.0 mg of dispersed MCNT, in 10 mL of EtOH

under ultrasonication for at least 10 minutes to form the precursor dispersion, into which a piece of NF was dipped to be coated with a layer of the precursor dispersion for a subsequent roasting process. The precursor dispersion enveloped NF (1.0 cm × 2.0 cm) (90 PPI, 1.7 mm in thickness) was placed 0.5 cm above the nozzle of a butane firing gas torch (Diarex Co., Ltd) to combust the solvent, EtOH, triggering the oxidation of $NiCl_2 \cdot 6H_2O$ and $MoCl_5$ to form intermediate precursors for Ni and Mo. The dip-and-roast process was repeated 30 times. The intermediate precursor coated NF was then calcined in an atmosphere of 5% H_2/Ar at 600 °C for 2 hours to afford the Mo_2C/NiMo heterostructured catalyst loaded NF, termed Mo_2C/NiMo@NF. The Mo_2C/NiMo loaded NF was cut into pieces of 0.5 cm × 0.5 cm for materials and electrochemical characterization. The catalyst mass loading on NF was estimated from the weight difference between the pristine NF and the catalyst loaded NF, to be about 30 mg cm^{-2}. The preparation procedures for Mo_2C/FeNiMo, Mo_2C, NiMo, and FeNiMo were the same with those of Mo_2C/NiMo, except for the formulae of the precursor dispersions. For Mo_2C/FeNiMo, the precursor dispersion was composed of $FeCl_2 \cdot 4H_2O$ (17.2 mM), $NiCl_2 \cdot 6H_2O$ (68.7 mM), $MoCl_5$ (68.7 mM), and 10.0 mg of MCNT. For Mo_2C, the precursor dispersion was composed of $MoCl_5$ (51.5 mM) and 20.0 mg of MCNT. For NiMo, the precursor solution was composed of $NiCl_2 \cdot 6H_2O$ (68.7 mM) and $MoCl_5$ (10.3 mM) without the presence of MCNT. For FeNiMo, the precursor solution contained $FeCl_2 \cdot 4H_2O$ (17.2 mM), $NiCl_2 \cdot 6H_2O$ (68.7 mM), and $MoCl_5$ (12.9 mM), without the presence of MCNT. For electrochemical characterization of the AEMWE, thin NF substrates (2.3 cm × 2.3 cm, 95 PPI, 0.3 mm in thickness) were used for loading of the catalyst to reduce the overall resistance of the device. Furthermore, the catalyst mass loading was reduced to 15 mg cm^{-2} for optimal electrochemical performances of the AEMWE. The catalyst loaded NF was cut into pieces of 2.0 cm × 2.0 cm for assembly of the AEMWE.

2.3. Fabrication of Pt/C and IrO_2 electrodes

Benchmark noble metal based cathode and anode materials, Pt/C for HER and IrO_2 for OER, respectively were fabricated with a drop-casting method. Commercial IrO_2 (or Pt/C) powder (10.0 mg) was dispersed in a 2.0 mL mixed solution containing ethanol (1.9 mL) and Nafion solution (0.1 mL), with the Nafion solution serving as a binder. The resulting suspension underwent ultrasonication for at least 1 hour to achieve a homogeneous catalyst ink. Subsequently, 20 μL of the IrO_2 (or Pt/C) catalyst ink was drop-cast onto a 0.5 cm × 0.5 cm piece of NF (90 PPI, 1.7 mm in thickness), followed by drying in an oven at 60 °C for 10 minutes. This procedure was repeated 20 times to attain a catalyst loading of 30.0 mg cm^{-2}.

2.4. Pre-treatment of anion exchange membranes

An anion exchange membrane was cut into pieces of 3.5 cm × 3.5 cm and immersed in 1.0 M KOH at room temperature for at least 24 hours to achieve complete conversion from the carbonate to hydroxide form in the AEM.

2.5. Assembly of anion exchange membrane water electrolyzer

The anion exchange membrane water electrolyzer (AEMWE) was composed of two stainless steel end plates, two gold-plated copper bipolar plates, two stainless steel flow fields, two PTFE gaskets, one Mo_2C/NiMo cathode (2 cm × 2 cm), one Mo_2C/FeNiMo anode (2 cm × 2 cm), and one activated AEM. The membrane electrode assembly (MEA) was fabricated by sandwiching the AEM between the Mo_2C/NiMo cathode and Mo_2C/FeNiMo anode, followed by pressing together the rest of the components from the inside out in the following order: gaskets, flow fields, bipolar plates, and end plates. The AEMWE was tightened using a digital torque wrench set at 1.2 N m. A 1.0 M KOH electrolyte was fed to the anode side at a flow rate of 30 mL min^{-1} for at least 10 hours to ensure complete membrane wetting prior to the measurements. The system temperature was controlled at 60 °C during operation.

2.6. Materials characterization

X-ray diffraction (XRD) patterns were recorded using a Bruker D8A25 diffractometer with Cu Kα radiation as the X-ray source. Elemental composition was determined by inductively coupled plasma optical emission spectroscopy (ICP-OES, Thermo Scientific iCAP 7200 Duo). Raman spectra were recorded using a Micro Raman Identify Dual system (PTT, MRID) with a 532 nm green laser as the light source. Sample morphology was examined with field-emission scanning electron microscopy (FE-SEM, HITACHI SU8010). Atomic structure and elemental distribution were characterized with high-resolution transmission electron microscopy (HRTEM, JEOL JEM-ARM200FTH), high-angle annular dark-field scanning transmission electron microscopy (HAADF-STEM), and energy dispersive X-ray spectroscopy (EDS). Surface oxidation states of the samples were probed with high-resolution X-ray photoelectron spectroscopy (HRXPS, ULVAC-PHI Quantera II) equipped with an Al X-ray source. X-ray absorption spectroscopy (XAS) measurements were conducted at the National Synchrotron Radiation Research Center (NSRRC), Taiwan. *Ex situ* and *in situ* XAS spectra of Fe, Ni, and Mo K-edges were collected at beamline TPS 44A1 in transmission mode under operation in a quick-scanning transmission mode.

2.7. Electrochemical characterization

Electrochemical characterization was conducted with a CHI6273E electrochemical workstation. The catalyst loaded NF serves as the working electrode (0.5 cm × 0.5 cm) with a blank NF (1 cm × 2 cm) and Hg/HgO (BAS Inc., RE-61AP) used as the counter and reference electrodes, respectively. The Hg/HgO reference electrode was pre-calibrated in 1.0 M KOH before use. Cyclic voltammetry (CV) was conducted for 30 cycles at 100 mV s^{-1} within potential windows of 0 to −0.4 V (*vs.* RHE) and 1.0 to 1.5 V (*vs.* RHE) for HER and OER, respectively to stabilize the catalysts. Linear sweep voltammetry (LSV) was conducted at 1 mV s^{-1} within the same potential windows, with 90% *iR*-compensation applied. Electrochemical impedance

spectroscopy (EIS) was conducted at −0.2 V (*vs.* RHE) and 1.58 V (*vs.* RHE) for HER and OER, respectively over the frequency range of 10 kHz to 0.01 Hz. Double-layer capacitance (C_{dl}) was estimated from CVs recorded within a non-faradaic potential window of 50 mV width at increasing scan rates of 10 to 50 mV s^{-1} at an interval of 10 mV s^{-1}.

2.8. AEMWE measurements

Electrochemical performances of AEMWEs were measured with a BioLogic HCP-803 potentiostat. CV was conducted within a voltage window of 1.2 to 1.8 V at 100 mV s^{-1} for 10 cycles prior to LSV measurements. The LSV was conducted at 1 mV s^{-1} from 1.2 to 2.0 V without application of *iR*-compensation. EIS was recorded at 1.8 V over a frequency range of 10 kHz to 0.1 Hz. Long-term stability was assessed at 0.5 A cm^{-2} for 50 hours.

3. Results and discussion

3.1. Materials characterization

The catalysts were prepared with a simple dip–roast–reduction method. Briefly, precursors, including metal salts and MCNTs, were first loaded onto a NF substrate through a dip-and-roast process, followed by a thermal reduction treatment to afford the product catalysts (Scheme S1). In addition to the carbide/alloy heterostructured catalysts, Mo_2C/NiMo for HER and Mo_2C/FeNiMo for OER, corresponding single component control catalysts, including Mo_2C, NiMo, and FeNiMo, were also prepared for comparison. Fig. 1a shows the XRD patterns of the five sample catalysts. Two characteristic sets of diffraction peaks are observed for the two heterostructured catalysts, one set (2θ of 34.6°, 38.2°, 39.6°, 52.4°, 61.8°, 69.7°, 74.9°, and 75.6°) corresponding to Mo_2C (COD-5910009)[21] and the other set (2θ of around 44°, 51°, and 76°) contributed by the respective face-centered cubic (FCC) alloy components, confirming the successful formation of Mo_2C/alloy heterostructured catalysts. Notably, no diffraction peaks associated with iron/nickel carbides are observed. This can be attributed to the much stronger binding affinity of Mo toward carbon as compared to those of Ni and Fe, making Mo the most favorable element among the three for carbide formation.[22] The intermediate precursors were reduced to form corresponding metals upon thermal reduction at 600 °C and part of the Mo reacts with carbon of the carbon source, here MCNT, for the formation of Mo_2C, whereas the rest of the Mo dissolves into the FCC Ni/Ni–Fe matrices to form NiMo/FeNiMo alloys. Note that the presence of Ni stabilizes the FCC structure even though the thermodynamically stable phases of Mo and Fe at low temperatures are both body-centered cubic (BCC). The phase fractions of Mo_2C and FCC-alloy in the two heterostructured catalysts were estimated by Rietveld refinement of the XRD spectra to be 36% Mo_2C and 64% FCC-NiMo for Mo_2C/NiMo and 29% Mo_2C and 71% FCC-FeNiMo for Mo_2C/FeNiMo. As for NiMo and FeNiMo, typical diffraction peaks of the FCC phase are observed, with no impurity peaks present, indicating the pure FCC nature of the two alloys. For Mo_2C, in addition to the characteristic diffraction peaks of Mo_2C, extra diffraction peaks associated with graphitic carbon and FCC Ni are also observed. The diffraction peak of graphitic carbon at 2θ of around 26° comes from the residual carbon source, MCNT, and those of Ni at 2θ of around 45°, 52°, and 77° is contributed by Ni contamination from the NF substrate when scraping Mo_2C from the NF substrate during the sample preparation step. The metallic compositions of the five sample catalysts, determined with ICP-OES, are summarized in Table S1 for comparison. Evidently, all alloy components are Ni based, ensuring their FCC crystalline phases.

Fig. 1b and c show the morphologies of Mo_2C/NiMo and Mo_2C/FeNiMo, respectively, with locally enlarged images shown in the insets for close examination. The morphologies of the control samples, Mo_2C, NiMo, and FeNiMo are displayed in Fig. S1 for comparison. Notably, the characteristic dimension of Mo_2C/FeNiMo (inset of Fig. 1c) is appreciably smaller than that of Mo_2C/NiMo (inset of Fig. 1b). Under similar synthetic conditions, FeNiMo alloys typically exhibit smaller product sizes than NiMo alloys because of enhanced lattice distortion and suppressed grain growth in the presence of an extra element, here Fe. Compared with the control samples, the two alloy control samples, NiMo (Fig. S1f) and FeNiMo (Fig. S1i), exhibit even larger characteristic dimensions than the two heterostructured catalysts. In the presence of Mo_2C, a material with an extremely high melting point (~2690 °C), the sintering of the alloys is obstructed, leading to smaller product sizes. The two heterostructured catalysts thus possess porous structures with finer structural features, resulting in higher surface areas that expose abundant accessible active sites for catalysis of the involved electrochemical reactions and consequently enhance electrocatalytic performances.

In addition to SEM imaging, HRTEM and STEM-EDS were conducted to investigate the detailed crystalline structure and elemental distributions of the sample catalysts. Fig. 1d–f present the HRTEM images and elemental distributions of Mo_2C/NiMo. As shown in Fig. 1e, the Mo_2C domain is identified from the (112) and (101) planes, showing interlayer distances of 0.13 and 0.23 nm, respectively. The angle contained between the two planes is measured to be 31.5°, in reasonable agreement with the theoretical value of 30°. As for the NiMo alloy domain, the interlayer distances of 0.21 and 0.18 nm are determined for the (211) and (130) planes, respectively, which contain an angle of 52°, in reasonable agreement with the theoretical value of 50°. Furthermore, STEM-EDS elemental mapping confirms that Ni, Mo, and C are uniformly distributed in the catalyst. Formation of the Mo_2C/NiMo heterostructure is thus confirmed. Fig. 1g–i show the HRTEM images and STEM-EDS elemental mapping of Mo_2C/FeNiMo. As shown in Fig. 1h, the Mo_2C domain exhibits the same lattice planes as observed in Mo_2C/NiMo, namely (112) and (101). For the FeNiMo alloy domain, the (130) and (420) planes are identified with the interlayer distances of 0.18 and 0.13 nm, respectively. The angle contained by the (130) and (420) planes is measured to be 46.7°, in reasonable agreement with the theoretical value of 45°. In addition, STEM-EDS elemental mapping (Fig. 1i) reveals uniform distributions of Fe, Ni, Mo, and C in the catalyst. These results confirm that Mo_2C/FeNiMo contains both Mo_2C and

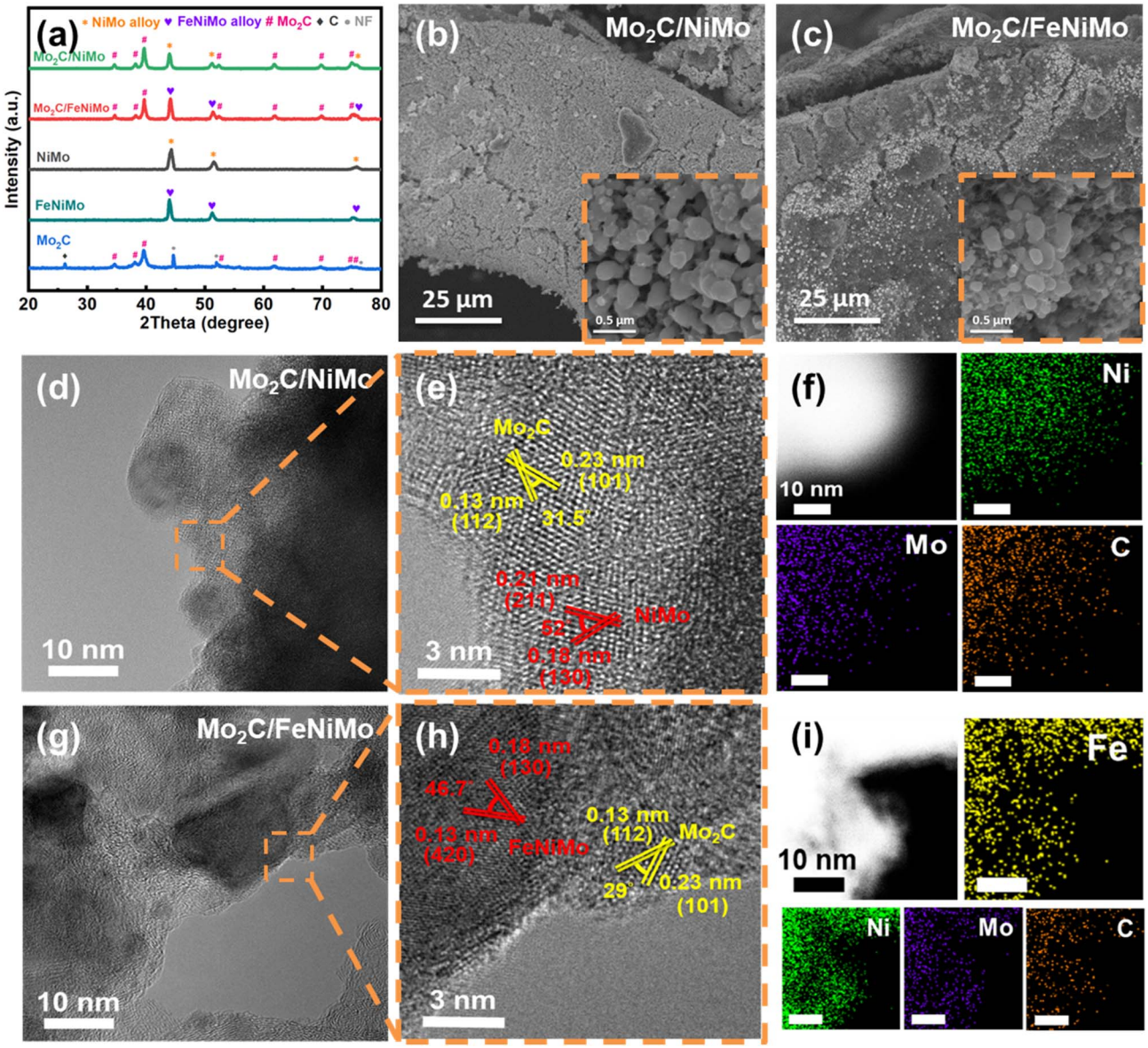

Fig. 1 (a) XRD patterns of Mo_2C/NiMo, Mo_2C/FeNiMo, NiMo, FeNiMo, and Mo_2C. (b and c) SEM images of Mo_2C/NiMo and Mo_2C/FeNiMo, respectively, with insets showing locally enlarged images. HR-TEM images, locally enlarged images showing lattice fringes, and corresponding STEM-EDS elemental mapping for (d–f) Mo_2C/NiMo and (g–i) Mo_2C/FeNiMo.

FeNiMo, thereby verifying the successful formation of the heterostructured catalyst.

The five sample catalysts were further characterized with XAS to examine the local structures and chemical states of their constituent elements. They were compared in two groups, the HER group containing Mo_2C/NiMo and its control samples, Mo_2C and NiMo, and the OER group containing Mo_2C/FeNiMo and its control samples, Mo_2C and FeNiMo. For the HER group, the X-ray absorption near-edge structure (XANES) spectra of the Ni K-edge and Mo K-edge are shown in Fig. 2a and b, respectively for comparison. Evidently, the absorption edge of the Ni K-edge of Mo_2C/NiMo shifts to a higher energy as compared with that of the control sample NiMo. This positive shift indicates a decrease in electron density around Ni, suggesting that Ni becomes more electron-deficient in the presence of Mo_2C. This can be attributed to the strong electronic interactions at the Mo_2C/NiMo interface, where charge transfer from Ni to the electron-withdrawing Mo_2C occurs. Note that carbon in Mo_2C polarizes the Mo–C bonds, rendering the Mo centers electronically deficient, thereby promoting electron donation from Ni. Fig. 2b shows the XANES spectra of the Mo K-edge of Mo_2C/NiMo, NiMo, and Mo_2C. Here, Mo exists in a metallic state in NiMo and in a low-valent, electron-deficient state in Mo_2C. Consequently, Mo_2C/NiMo, which contains Mo in both chemical states, exhibits an absorption edge positioned between those of NiMo and Mo_2C.

Fig. 2c and d show the corresponding Fourier-transformed extended X-ray absorption fine structure (FT-EXAFS) spectra of

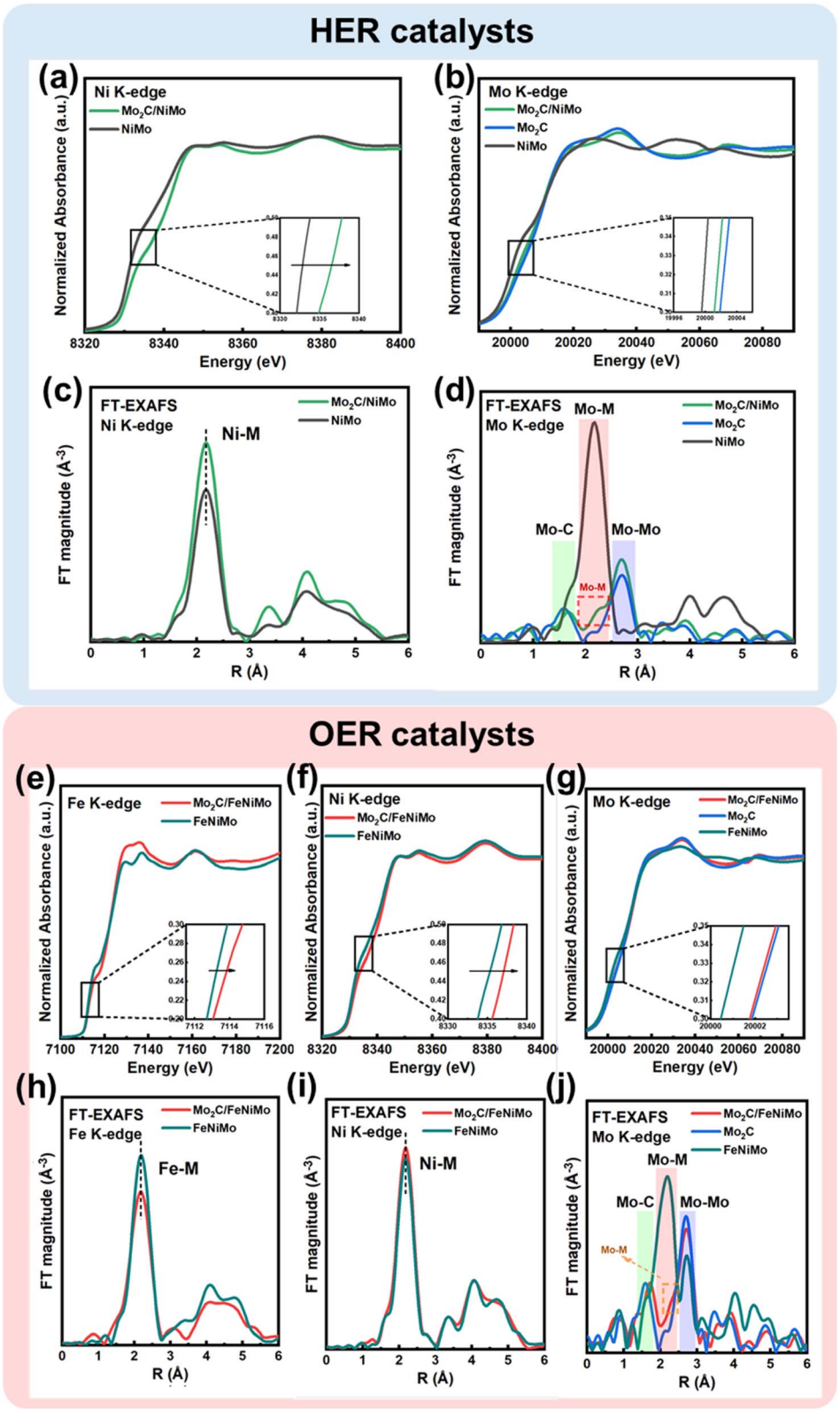

Fig. 2 (a and b) XANES and (c and d) k^2-weighted FT-EXAFS spectra of Ni and Mo K-edges of Mo_2C/NiMo, Mo_2C, and NiMo. (e–g) XANES and (h–j) k^2-weighted FT-EXAFS spectra of Fe, Ni, and Mo K-edges of Mo_2C/FeNiMo, Mo_2C, and FeNiMo. Insets in XANES spectra show locally enlarged absorption edges.

Ni and Mo K-edges, respectively. The first coordination shell of the Ni K-edge is located at around 2.2 Å, accounting for the coordination of Ni with its nearest neighboring metal atoms, Ni and Mo, denoted as Ni–M,[23,24] for both Mo_2C/NiMo and NiMo. As for the Mo K-edge, the FT-EXAFS spectrum of NiMo is distinctly different from those of Mo_2C/NiMo and Mo_2C. For NiMo, the first coordination shell is located at around 2.2 Å, accounting for the coordination of Mo with its nearest neighboring metal atoms, Mo and Ni, denoted as Mo–M.[23,24] As for Mo_2C/NiMo and Mo_2C, the first coordination shell is located at around 1.7 and 1.6 Å, respectively, accounting for the Mo–C bonds in Mo_2C. Note that the Mo–C bond in Mo_2C/NiMo is slightly longer than that in Mo_2C. For Mo_2C/NiMo, it is inferred from Fig. 2a that electrons flow from Ni to Mo_2C in Mo_2C/NiMo, rendering Mo in Mo_2C of Mo_2C/NiMo more electron-rich as compared with Mo in plain Mo_2C. The enhanced electron–electron repulsion between electron-rich Mo and electron-rich C thus lengthens the Mo–C bond. The second coordination shell is located at around 2.7 Å, attributable mainly to the Mo–Mo bond in Mo_2C,[25,26] with a low-intensity shoulder located at 2.2 Å accounting for the Mo–M (M = Ni, Mo) bond in NiMo.

For the OER group, the characteristic features of the XANES and FT-EXAFS spectra are similar to those of the HER group. The XANES spectra of Fe and Ni K-edges are displayed in Fig. 2e and f, respectively. The absorption edges of Fe and Ni K-edges of Mo_2C/FeNiMo both shift to higher energies as compared with those of FeNiMo, indicating electron transfer from Fe and Ni to Mo_2C. As for the Mo K-edge (Fig. 2g), the absorption edge of Mo_2C/FeNiMo also positions between those of FeNiMo and Mo_2C because of the mixed chemical states of Mo in the composite. For the corresponding FT-EXAFS spectra, the first coordination shells of Fe and Ni K-edges (Fig. 2h and i) are both located at around 2.2 Å, accounting for the coordination of Fe and Ni with their nearest neighboring metal atoms, Fe, Ni, and Mo, denoted as Fe–M and Ni–M,[23,24] for both Mo_2C/FeNiMo and FeNiMo. As for the Mo K-edge (Fig. 2j), the FT-EXAFS spectrum of FeNiMo is distinctly different from those of Mo_2C/FeNiMo and Mo_2C. For FeNiMo, the first coordination shell is located at around 2.2 Å, accounting for the coordination of Mo with its nearest neighboring metal atoms, Mo, Fe, and Ni, denoted as Mo–M.[23,24] As for Mo_2C/FeNiMo and Mo_2C, the first coordination shell is located at around 1.7 and 1.6 Å, respectively, similar to the situation observed for Mo_2C/NiMo (Fig. 2d), accounting for the Mo–C bonds in Mo_2C. The second coordination shell is located at around 2.7 Å, attributable mainly to the Mo–Mo bond in Mo_2C,[25,26] with a low-intensity shoulder located at 2.2 Å accounting for the Mo–Fe/Ni bond in FeNiMo.[25,26] Overall, the XAS measurements indicate that both Mo_2C/NiMo and Mo_2C/FeNiMo possess the characteristic features of the carbide/alloy heterostructure, thereby further confirming the successful formation of the carbide/alloy heterostructured catalysts.

3.2. Surface characterization

High-resolution X-ray photoelectron spectroscopy (HRXPS) was conducted to further investigate the surface chemical states and electronic structure of the sample catalysts. Fig. 3a–c display the HRXPS spectra of Ni 2p, C 1s, and Mo 3d, respectively for Mo_2C/NiMo, along with those of the two control samples, Mo_2C and NiMo. These spectra provide insights into the electronic interactions between Mo_2C and NiMo within the Mo_2C/NiMo heterostructure. The Ni 2p spectra (Fig. 3a) show the characteristic spin–orbit doublets of Ni $2p_{3/2}$ and Ni $2p_{1/2}$, along with their associated satellite features. The Ni 2p spectra can be deconvoluted into three main constituent peaks: Ni^0, Ni^{2+}, and the satellite.[27,28] The presence of Ni^0 indicates the existence of metallic nickel in the samples, whereas the Ni^{2+} signal originates from surface oxidation of the samples upon exposure to an ambient atmosphere. The detailed characteristic binding energies of Ni 2p are summarized in Table S2 for comparison. By comparison, the Ni 2p peaks of Mo_2C/NiMo exhibit a slight positive shift in binding energies as compared with those of NiMo, consistent with the relevant finding derived from the XANES spectra of the Ni K-edge (Fig. 2a), confirming electron transfer from Ni to Mo_2C in Mo_2C/NiMo. In the C 1s spectra (Fig. 3b), four characteristic peaks can be identified from the broad envelop spanning from 283 to 291 eV through deconvolution. The four peaks are contributed by the Mo–C, C–C/C–H, C–O, and C=O bonds[29–31] in order of increasing binding energies (Table S3). The presence of the carbidic carbon bond, Mo–C, confirms the formation of Mo_2C, whereas the C–C/C–H, C–O, and C=O peaks are from the organic surface contaminants deposited upon exposure of the sample to an ambient atmosphere. The binding energies of the Mo–C peaks of Mo_2C/NiMo and Mo_2C are the same (Table S3), suggesting that the chemical environment and electronic state of the carbidic carbon remain essentially unchanged upon integration of Mo_2C with NiMo alloy for the formation of the Mo_2C/NiMo heterostructure. This outcome can be attributed to the covalent nature of the Mo–C bonding, in which electrons are more localized compared to metallic bonding, thus limiting their susceptibilities to neighboring electronic perturbations. Moreover, the alloy phase does not directly bond with the carbon in Mo_2C of Mo_2C/NiMo, making it less likely to induce significant changes in the electron density of the carbon. Fig. 3c shows the HRXPS spectra of Mo 3d, which can be deconvoluted into four constituent components, including Mo^0, Mo^{2+}, Mo^{4+}, and Mo^{6+} in increasing binding energies[32,33] (Table S4). Besides the dominant Mo^{2+} from Mo_2C and metallic Mo from NiMo, because of the high susceptibility (low reduction potential) of Mo to oxidation, higher valence species, Mo^{4+} and Mo^{6+}, formed from the surface oxidation of the sample upon exposure to an ambient atmosphere, are also observed. It is evident from Table S4 that the Mo 3d peaks in Mo_2C/NiMo exhibit a slight negative shift as compared with those of Mo_2C and NiMo, suggesting that Mo in Mo_2C of Mo_2C/NiMo gains electrons from Ni in NiMo of Mo_2C/NiMo. Based on the above XPS analyses, it can be concluded that electron transfer occurs from the NiMo domain toward the Mo_2C domain within the Mo_2C/NiMo heterostructure. Such electron transfer highlights the electronic synergy between Mo_2C and NiMo, by which the binding strength between the catalyst surface and adsorbed hydrogen (H_{ads}) is modulated to facilitate hydrogen desorption and thus H_2 evolution, thereby enhancing the HER catalytic activity.[34,35]

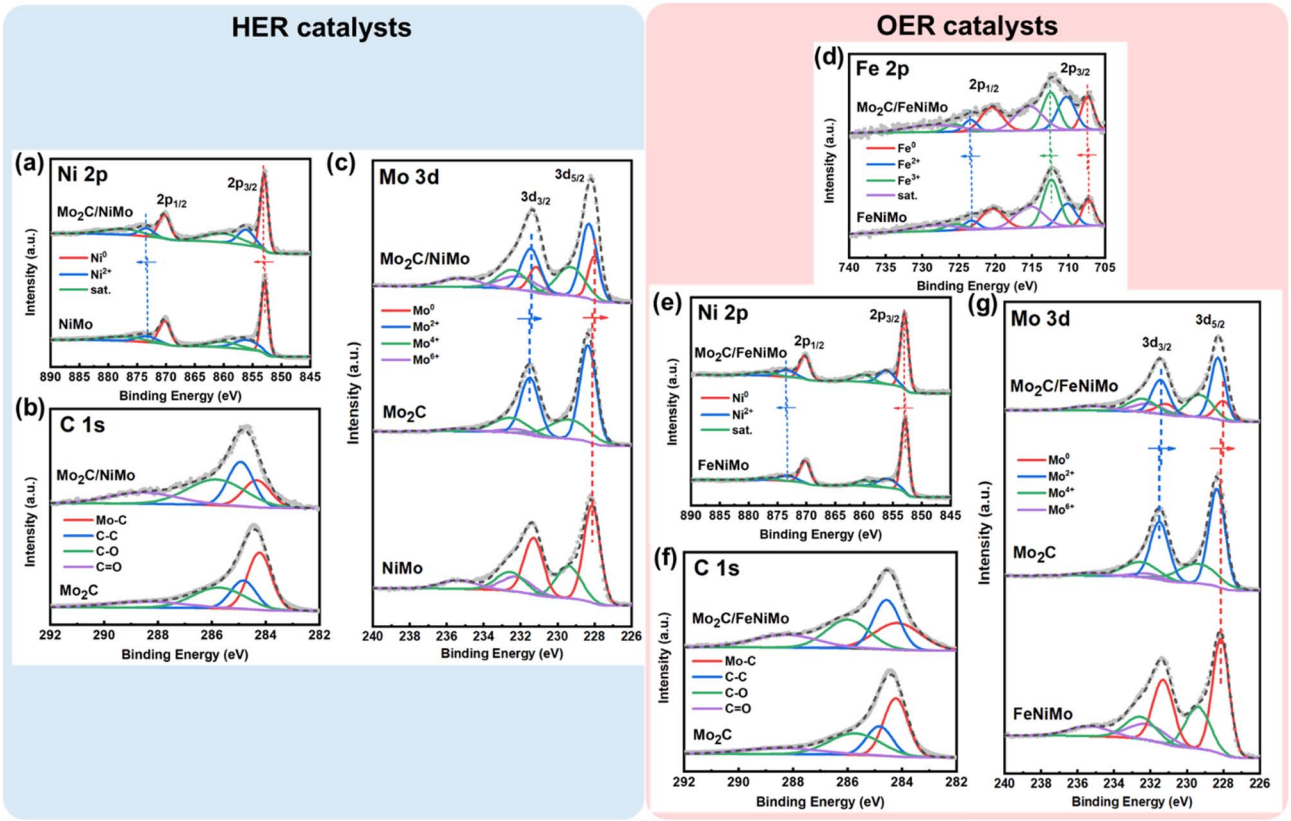

Fig. 3 HRXPS spectra of (a) Ni 2p, (b) C 1s, and (c) Mo 3d for Mo_2C/NiMo, Mo_2C, and NiMo. HRXPS spectra of (d) Fe 2p, (e) Ni 2p, (f) C 1s, and (g) Mo 3d for Mo_2C/FeNiMo, Mo_2C, and FeNiMo.

Fig. 3d–g show the HRXPS spectra of Fe 2p, Ni 2p, C 1s, and Mo 3d for Mo_2C/FeNiMo, together with those of the two control samples, Mo_2C and FeNiMo. The HRXPS spectra of Fe 2p (Fig. 3d) reveal the presence of three chemical states of Fe, namely metallic Fe (Fe^0), Fe^{2+}, and Fe^{3+}, along with the satellite peaks[36,37] in order of increasing binding energies (Table S5) for both Mo_2C/FeNiMo and FeNiMo. The presence of Fe^{2+} and Fe^{3+} is again attributed to the surface oxidation of the samples. The Fe 2p peaks of Mo_2C/FeNiMo exhibit a slight positive shift in binding energies as compared with those of FeNiMo, consistent with the relevant finding derived from the XANES spectra of the Fe K-edge (Fig. 1e), confirming electron transfer from Fe to Mo_2C in Mo_2C/FeNiMo. The Ni 2p spectra (Fig. 3e) exhibit characteristic signals of Ni^0 and Ni^{2+}, along with the satellite peaks,[27,28] in order of increasing binding energies (Table S6) for both Mo_2C/FeNiMo and FeNiMo. Similarly, the Ni 2p peaks of Mo_2C/FeNiMo exhibit a slight positive shift in binding energies as compared with those of FeNiMo, consistent with the relevant finding derived from the XANES spectra of the Ni K-edge (Fig. 2f), confirming electron transfer from Ni to Mo_2C in Mo_2C/FeNiMo. The C 1s spectrum (Fig. 3f) can be deconvoluted into four main peaks, corresponding to Mo–C, C–C, C–O, and C=O bonds, in order of increasing binding energies (Table S7). Similar to the case of Mo_2C/NiMo, no peak position shifts are observed for the Mo–C bond of Mo_2C/FeNiMo, indicating that the electronic environment of the carbidic carbon remains unchanged in Mo_2C/FeNiMo as compared to that in Mo_2C. This observation suggests that the covalent nature of the Mo–C bonding restricts electron redistribution, and that the integration of Mo_2C with FeNiMo does not alter the electronic states of the carbon in Mo_2C. Fig. 3g shows the HRXPS spectra of Mo 3d, which are composed of four characteristic peaks, namely metallic Mo (Mo^0), Mo^{2+}, Mo^{4+}, and Mo^{6+}, in order of increasing binding energies (Table S8). The Mo 3d peaks in Mo_2C/FeNiMo exhibit a slight negative shift as compared with those of Mo_2C and FeNiMo, suggesting that Mo in Mo_2C of Mo_2C/FeNiMo gains electrons from Fe and Ni in FeNiMo of Mo_2C/FeNiMo. Based on the above analyses, a finding similar to that observed in Mo_2C/NiMo is obtained. Within the Mo_2C/FeNiMo heterostructure, Fe and Ni in FeNiMo transfer electrons to Mo_2C, resulting in positive shifts of the characteristic binding energies of Fe and Ni, whereas the characteristic binding energies of Mo decrease accordingly. The presence of abundant Mo_2C/FeNiMo heterointerfaces facilitates such electron transfer, which modulates the adsorption/desorption energies of oxygen-containing species and optimizes the energy difference of the thermodynamic limiting steps of OER to enhance the OER performance of Mo_2C/FeNiMo.

3.3. Electrochemical characterization

The electrochemical performances of the five sample catalysts toward both HER and OER were characterized with a three-

electrode system in 1.0 M KOH. To ensure the accuracy of potential measurements, the Hg/HgO reference electrode was calibrated before use, as illustrated in Fig. S2. Linear sweep voltammetry and electrochemical impedance spectroscopy were conducted for all sample catalysts, with commercial noble metal based catalysts as benchmarks for comparison, Pt/C for HER and IrO_2 for OER.

Evident from the LSV polarization curves (Fig. 4a), the catalytic efficiency of the sample catalysts toward HER follows the trend: Mo_2C/NiMo > Mo_2C > Mo_2C/FeNiMo > NiMo > FeNiMo. Among the five sample catalysts, the Mo_2C/NiMo heterostructure exhibits the best catalytic performance toward HER, achieving current densities of 10 and 500 mA cm^{-2} at overpotentials of 37 (η_{10}) and 169 mV (η_{500}), respectively and a mass activity of 0.63 A g^{-1} at η of 50 mV. As a comparison, the corresponding single component catalysts, Mo_2C and NiMo, exhibit lower HER catalytic efficiency as compared to that of Mo_2C/NiMo, clearly demonstrating the positive synergy between Mo_2C and NiMo to boost the HER catalytic efficiency of Mo_2C/NiMo. Interestingly, inclusion of Fe in Mo_2C/NiMo leads to reduction in HER activities of Mo_2C/NiMo, even inferior to that of plain Mo_2C. This phenomenon can be attributed to the strong oxophilicity of Fe, leading to excessive OH adsorption and thus impeding H adsorption/desorption. Mo_2C/NiMo also shows the lowest Tafel slope of 74.6 mV dec^{-1} (Fig. 4b), indicating its relatively fast HER kinetics among the three sample catalysts. With a Tafel slope falling in between 120 and 40 mV dec^{-1}, it implies comparable Volmer (120 mV dec^{-1}, electrochemical hydrogen adsorption: $* + H_2O + e^- \rightarrow H^* + OH^-$) and Heyrovsky steps (40 mV dec^{-1}, electrochemical hydrogen desorption: $H^* + H_2O + e^- \rightarrow H_2 + OH^- + *$), both involving water dissociation, as the thermodynamic rate-determining step of the HER process.[38] As for the catalytic performances toward catalysis of OER, the OER catalytic efficiency follows the trend: Mo_2C/FeNiMo > FeNiMo > Mo_2C/NiMo ≈ Mo_2C > NiMo (Fig. 4b). Again, the results clearly demonstrate the positive

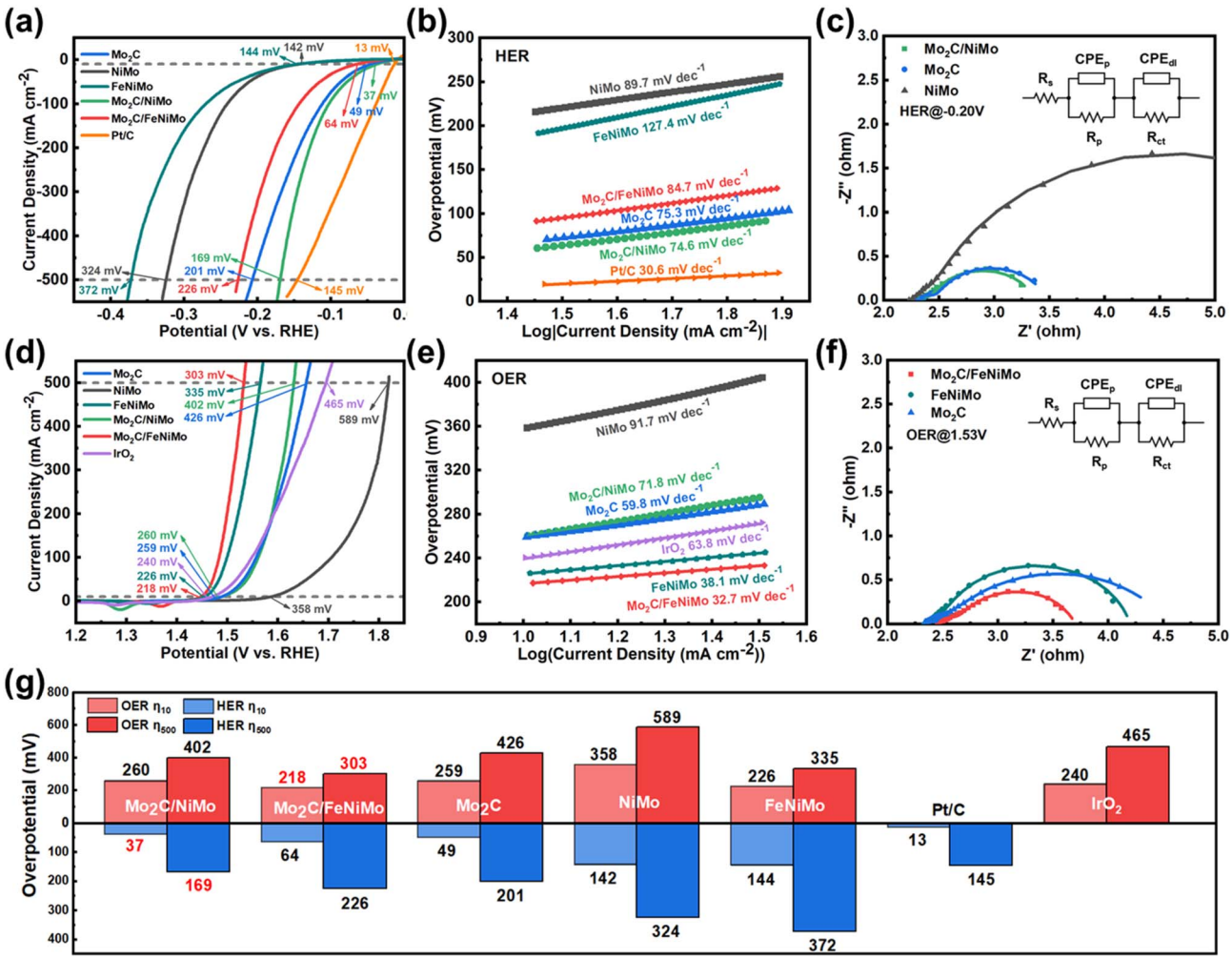

Fig. 4 Electrochemical characterization of Mo_2C/NiMo, Mo_2C/FeNiMo, Mo_2C, NiMo, and FeNiMo in 1.0 M KOH: (a) HER LSV curves, (b) HER Tafel plot, (c) Nyquist plot for HER recorded at −0.2 V (*vs.* RHE), (d) OER LSV curves, (e) OER Tafel plot, (f) Nyquist plot for OER recorded at 1.53 V (*vs.* RHE), and (g) summary of η_{10} and η_{500} of HER and OER. The Nyquist plot was fitted using an equivalent circuit model consisting of a series system resistance (R_s) and two parallel *R*–CPE branches: one with a porosity related constant phase element (CPE_p) and resistance (R_p), and the other with a double layer capacitance related constant phase element (CPE_{dl}) and charge transfer resistance (R_{ct}).

synergy between Mo_2C and FeNiMo to boost the OER catalytic efficiency of Mo_2C/FeNiMo. The Mo_2C/FeNiMo heterostructure exhibits the best OER performance, achieving current densities of 10 and 500 mA cm^{-2} at overpotentials of 218 (η_{10}) and 303 mV (η_{500}), respectively (Fig. 4d) and a mass activity of 15.9 A g^{-1} at η of 300 mV. Here, inclusion of Fe to Mo_2/NiMo boosts the OER activities of Mo_2C/NiMo, even superior to that of plain FeNiMo. This phenomenon can again be attributed to the strong oxophilicity of Fe, stabilizing the OER-active oxygenated intermediates and accelerating the high-valence redox transitions required for high OER activities. Mo_2C/FeNiMo also shows the lowest Tafel slope of 32.7 mV dec^{-1} (Fig. 4e), highlighting its fast OER kinetics. The overpotentials and Tafel slopes of all characterized samples toward HER and OER are summarized in Fig. 4g for comparison. Evidently, for overall water electrolysis, the coupling of Mo_2C/NiMo and Mo_2C/FeNiMo as the cathode and anode catalysts, respectively gives the lowest total overpotential of 472 mV at 500 mA cm^{-2}, a commercially relevant operating current density, largely outperforming 610 mV achieved by the Pt/C//IrO_2 couple. One concludes from the above observations that the positive synergy between the single component catalysts, Mo_2C and NiMo/FeNiMo, enhances the catalytic efficiency of the resulting heterostructured catalysts toward both HER and OER.

EIS measurements were conducted at −0.2 and 1.53 V (*vs.* RHE) (Fig. 4c and f) to further examine the reaction kinetics toward HER and OER, respectively. Nyquist plots were fitted with an equivalent circuit model (insets of Fig. 4c and f for HER and OER, respectively)[39] to determine the values of charge transfer resistances (R_{ct}). The fitting results are summarized in Tables S9 and S10 for HER and OER, respectively for comparison. The lowest R_{ct} values for HER and OER are achieved by Mo_2C/NiMo and Mo_2C/FeNiMo, respectively, in line with the outcomes of overpotentials and Tafel slopes. This highlights that heterostructured catalysts, relative to their single component counterparts, offer superior electron transfer efficiency at the catalyst–electrolyte interface and thus higher catalytic efficiency.

Double-layer capacitances (C_{dl}s), in direct proportionality to electrochemical active surface areas (ECSAs), were determined from cyclic voltammograms recorded within non-faradaic potential windows at increasing scan rates to serve as a quantitative measure of the quantity of exposed active sites for assessment of the intrinsic catalytic efficiency of the sample catalysts. The C_{dl}s of the sample catalysts are shown in Fig. S3a, with the corresponding plots of scan rates *versus* current density differences presented in Fig. S3b–f. The magnitudes of the C_{dl}s follow the decreasing order of Mo_2C/FeNiMo (161.7 mF cm^{-2}) > Mo_2C (155.6) > Mo_2C/NiMo (140.2) > FeNiMo (9.9) > NiMo (8.2). It is evident that the carbide containing samples exhibit significantly higher C_{dl}s as compared with those achieved by the alloy samples without the presence of carbides. Carbonaceous materials are known to possess good electrical conductivities and large specific surface areas, which facilitate ion adsorption/desorption for high C_{dl}s. From the comparison of the C_{dl}s of the five sample catalysts, it is evident that Mo_2C is the major contributor to the C_{dl}s of the two heterostructured catalysts, with the alloys contributing only very limited C_{dl}s.

The catalytic efficiency of a catalyst is mainly determined by the quantity and quality of the active sites of the catalyst. The effect of the quantity of the active sites may be excluded through normalization of the LSV curve with C_{dl} to give a qualitative measure of the intrinsic activity of the active sites of the catalyst, provided that the main contributor to the C_{dl} of the catalyst is also the main contributor of the catalytic efficiency of the catalyst. For HER, the catalytic efficiency of Mo_2C is close to that of Mo_2C/NiMo (Fig. 4a), indicating that Mo_2C is the main contributor to the catalytic efficiency of Mo_2C/NiMo. Nevertheless, for OER, the catalytic efficiency of FeNiMo, instead of Mo_2C, is close to that of Mo_2C/FeNiMo (Fig. 4d), indicating that FeNiMo, instead of Mo_2C, is the main contributor to the catalytic efficiency of Mo_2C/FeNiMo. Recall that Mo_2C is the main contributor to the C_{dl}s of both Mo_2C/NiMo and Mo_2C/FeNiMo. Consequently, the approach of C_{dl}-normalization for intrinsic activity assessment would give reliable results for HER catalyzed by Mo_2C/NiMo, but may not work properly for OER catalyzed by Mo_2C/FeNiMo. The C_{dl}-normalized LSV curves are presented in Fig. S4a and b for HER and OER, respectively for comparison. From Fig. S4a, it is evident that Mo_2C/NiMo exhibits the best intrinsic activity, outperforming its single component counterparts, Mo_2C and NiMo. As for OER, Fig. S4b shows that FeNiMo possesses the highest intrinsic activity, even higher than that of Mo_2C/FeNiMo. Here, Mo_2C, the main contributor to the C_{dl} of Mo_2C/FeNiMo, does not exhibit high OER activities, thereby rendering the C_{dl} of Mo_2C/FeNiMo an inappropriate parameter to account for the ECSA of Mo_2C/FeNiMo and C_{dl}-normalization an inappropriate approach for assessment of the intrinsic OER activity of Mo_2C/FeNiMo.

The best performing catalysts for HER, Mo_2C/NiMo, and OER, Mo_2C/FeNiMo, were coupled as the cathode and anode catalysts for overall water splitting in 1 M KOH. For comparison purposes, cathode//anode couples of Mo_2C/NiMo//FeNiMo, Mo_2C/NiMo//Mo_2C, NiMo//Mo_2C/FeNiMo, and Mo_2C//Mo_2C/FeNiMo were also characterized. Fig. 5a shows the polarization curves recorded for all sample couples for overall water splitting. Evidently, the Mo_2C/NiMo//Mo_2C/FeNiMo couple is the champion couple, requiring voltages of only 1.482 (*i.e.*, overpotential of 252 mV) and 1.709 V (*i.e.*, overpotential of 479 mV) to reach current densities of 10 and 500 mA cm^{-2}, respectively, outperforming all other couples. Overall, the catalytic efficiency of the five couples for overall water splitting is consistent with that of the combined corresponding hydrogen evolution and oxygen evolution half reactions.

The electrochemical performance of the sample catalysts was further characterized in an anion exchange membrane water electrolysis (AEMWE) system. The Mo_2C/NiMo@NF and Mo_2C/FeNiMo@NF electrodes were used as the cathode and anode, respectively, sandwiching a PiperION anion exchange membrane, to form an AEMWE cell, denoted as Mo_2C/NiMo@NF//PiperION//Mo_2C/FeNiMo@NF. For comparison purposes, AEMWE cells of Mo_2C/NiMo//PiperION//FeNiMo, Mo_2C/NiMo//PiperION//Mo_2C, NiMo//PiperION//Mo_2C/FeNiMo, and Mo_2C//PiperION//Mo_2C/FeNiMo were also

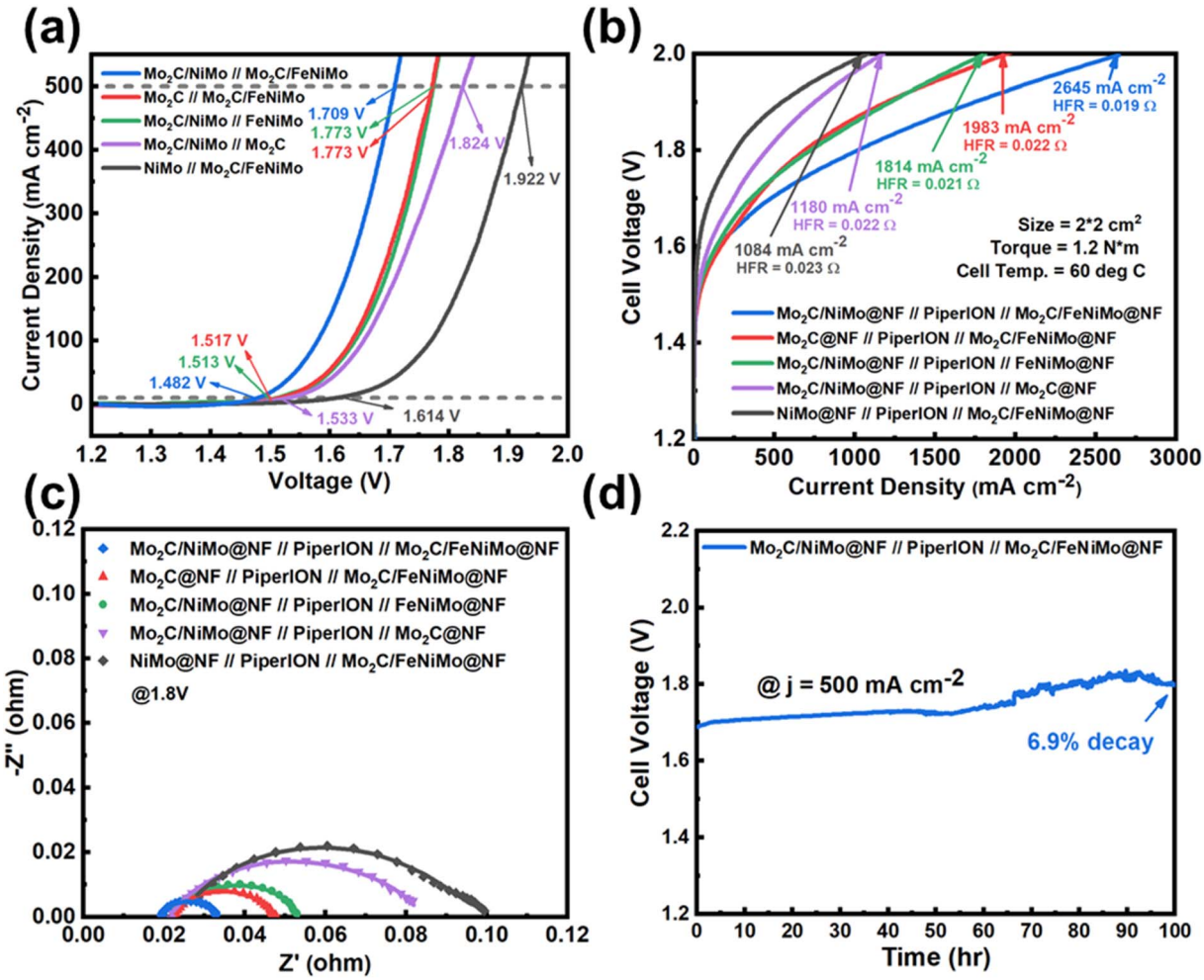

Fig. 5 (a) LSV curves recorded for overall water splitting of five HER catalyst//OER catalyst couples in 1 M KOH. (b) Polarization curves recorded for five AEMWEs with cathode//PiperION//anode membrane electrode assembly. (c) Nyquist plots recorded at a cell voltage of 1.8 V for five AEMWEs. (d) Chronopotentiometric stability test at 0.5 A cm^{-2} for 100 hours for the Mo_2C/NiMo@NF//PiperION//Mo_2C/FeNiMo@NF based AEMWE. For Nyquist plots, all experimental data are plotted in symbols, with fitting results drawn as solid lines. The equivalent circuit model in panel (c) comprises a high frequency resistance (R_0), two charge transfer resistances (R_1 and R_2), and two constant-phase element capacitors (CPE_1 and CPE_2).

assembled and characterized. All electrochemical characterization studies were conducted at 60 °C with a 1.0 M KOH solution circulated through the anode side. The performance of the AEMWEs is shown in Fig. 5b. Evidently, the Mo_2C/NiMo@NF//PiperION//Mo_2C/FeNiMo@NF based AEMWE exhibits the best water electrolysis performance, delivering a current density as high as 2.645 A cm^{-2} at a cell voltage of 2.0 V without *iR* compensation. Overall, the performance trend of the five AEMWEs is consistent with that observed from the corresponding overall water splitting characterization in aqueous media (Fig. 5a), confirming that the overall water splitting performance observed in aqueous media is faithfully reflected in the corresponding AEMWE system. Table S11 summarizes electrochemical performances of the Mo_2C/NiMo//PiperION//Mo_2C/FeNiMo based AEMWE as compared with those of state-of-the-art non-precious transition metal catalysts based AEMWEs reported in recent years. Evidently, the Mo_2C/NiMo//PiperION//Mo_2C/FeNiMo based AEMWE stands out strongly.

EIS measurements were conducted on the five AEMWEs at a cell voltage of 1.8 V (Fig. 5c) to examine internal resistances involved in operation of the AEMWE's. The recorded Nyquist plots are fitted with an equivalent circuit model (inset of Fig. 5c) to determine the values of high frequency resistance (HFR) and charge transfer resistances (R_1 for HER and R_2 for OER), as summarized in Table S12 for comparison. For the HFR, which mainly accounts for ionic resistance of the electrolyte, electronic resistances of the cathode and anode, and contact resistances between components, all five AEMWEs exhibit similar values around 0.021 Ω, implying consistency in cell assembly. As for the two charge transfer resistances, one for the HER at the cathode and the other for the OER at the anode, the values correlate well with the HER/OER catalytic efficiency of the catalysts characterized in 1 M KOH (Fig. 4a and d): the lower charge transfer resistance corresponds to higher catalytic efficiency. Consequently, the Mo_2C/NiMo//PiperION//Mo_2C/FeNiMo based AEMWE exhibits the lowest R_1 of 0.0110 Ω and

R_2 of 0.0145 Ω. And together with its lowest HFR of 0.019 Ω, the Mo_2C/NiMo//PiperION//Mo_2C/FeNiMo based AEMWE delivers the highest current density of 2.645 A cm^{-2} at 2.0 V, with the Mo_2C//PiperION//Mo_2C/FeNiMo based AEMWE coming next, followed by the Mo_2C/NiMo//PiperION//FeNiMo based AEMWE, Mo_2C/NiMo//PiperION//Mo_2C based AEMWE, and NiMo//PiperION//FeNiMo based AEMWE in decreasing order.

Fig. 5d shows the long-term durability of the Mo_2C/NiMo@NF//PiperION//Mo_2C/FeNiMo@NF based AEMWE, characterized in a chronopotentiometric mode at a commercially relevant constant current density of 0.5 A cm^{-2} for 100 h. The cell exhibits a 6.9% performance decay, demonstrating its good operational stability and promising potential for green hydrogen production.

To further examine the electrochemical stability of the HER catalyst, Mo_2C/NiMo, and the OER catalyst, Mo_2C/FeNiMo, chronopotentiometric stability tests were conducted at 0.5 A cm^{-2} for 50 hours in 1 M KOH (Fig. S5a and b). Evidently, both Mo_2C/NiMo and Mo_2C/FeNiMo outperform their noble metal based benchmark catalysts, Pt/C for HER (0.7 *vs.* 4.2% decay) and IrO_2 for OER (2.4 *vs.* 4.5% decay). The catalysts after the stability tests were collected for XPS (Fig. S6 and S7) characterization to examine the material stability of the catalysts. The combined surface contents of alloy and Mo_2C on the catalyst are estimated as the ratio of signal peak areas of (Ni^0 + Mo^0 + Mo^{2+}) *versus* (Ni^0 + Ni^{2+} + Mo^0 + Mo^{2+} + Mo^{4+} + Mo^{6+}) for Mo_2C/NiMo (Table S13) and (Fe^0 + Ni^0 + Mo^0 + Mo^{2+}) *versus* (Fe^0 + Fe^{2+} + Fe^{3+} + Ni^0 + Ni^{2+} + Mo^0 + Mo^{2+} + Mo^{4+} + Mo^{6+}) for Mo_2C/FeNiMo (Table S14). Comparison of this ratio before and after the stability test reveals the stability of the surface composition of the catalyst against HER and OER operations in corrosive alkaline media. Evidently, even under cathodic bias, corrosive leaching of surface Ni and Mo occurs after prolonged HER operation in alkaline media. As for the prolonged OER operation, surface oxidation for formation of OER-active intermediates, together with corrosive leaching, results in complete removal of zero/low valent species of Fe, Ni, and Mo under anodic bias in alkaline media.

3.4. *In situ* analyses

In situ characterization studies, including X-ray absorption spectroscopy and Raman spectroscopy, were conducted to gain insights into the electronic and structural changes of the sample catalysts during HER and OER for mechanistic understanding. In the case of *in situ* XAS, variations in XANES and FT-EXAFS spectra are recorded as the applied potential is altered, thereby revealing changes in valence states and local coordination environments of the constituent elements of the sample catalysts. In parallel, *in situ* Raman spectroscopy monitors the evolution of vibrational and rotational features under varying applied potentials, offering information on the formation of surface active intermediates during HER and OER.

In situ XAS measurements were conducted on the two best performing catalysts, Mo_2C/NiMo for HER and Mo_2C/FeNiMo for OER. Fig. 6a and b show the *in situ* XANES spectra of Ni and Mo K-edges of Mo_2C/NiMo under HER conditions. When the applied potential is reduced from the open circuit potential (OCP) to −0.2 V, the absorption edge of the Ni K-edge exhibits no noticeable shifts, whereas that of the Mo K-edge shifts toward lower energies. This indicates that the average oxidation state of Ni remains essentially unchanged during the HER and the Mo species become more electron-rich under the cathodic bias. When the applied potential returns to OCP, the absorption edge of the Mo K-edge shifts back to its original position, indicating the reversibility of the cathodic bias induced electron flow. Fig. S8a displays the FT-EXAFS spectra of the Ni K-edge, showing a prominent first coordination shell located at around 2.2 Å, corresponding to Ni–M coordination (M = Ni or Mo).[40] Upon application of a reduction potential at −0.2 V, the shell intensity drops slightly as shown in the inset of Fig. S8a, indicating increased local disorder and thus decreased coordination of Ni. As inferred from the value of the Tafel slope of Mo_2C/NiMo toward HER catalysis (Fig. 4b), the HER proceeds *via* the Volmer–Heyrovsky route, in which water dissociation is critically involved. Ni is active toward water dissociation catalysis,[41] in which dynamic adsorption of H_2O and subsequent formation of Ni*–H and Ni*–OH transiently perturb the local coordination environment of Ni, increasing local disorder and thus reducing the coordination shell intensity. Upon returning the applied potential back to OCP, the shell intensity returns to its initial state, resulting from cessation of the participation of Ni in water dissociation catalysis. Fig. S8b shows the FT-EXAFS spectra of the Mo K-edge of Mo_2C/NiMo. The pronounced coordination shell located at 1.7 Å corresponds to the Mo–C bond of the Mo_2C phase. Under HER conditions at −0.2 V, the coordination shell intensity is slightly increased. At −0.2 V, Mo becomes electron-rich (Fig. 6b), which stabilizes and increases ordering of the Mo_2C phase to strengthen Mo–C coordination for the coordination shell intensity increase observed. When the applied potential is returned to OCP, the coordination shell intensity returns to the initial state, resulting from the reversible cathodic bias induced electron flow. In the Mo_2C/NiMo heterostructured catalyst, H* generated on Ni sites during the Volmer step can migrate to nearby Mo_2C sites *via* a spillover process. Hydrogen spillover mainly proceeds from sites of stronger hydrogen adsorption, advantageous for H* generation from water dissociation, to sites of weaker hydrogen adsorption.[42] Here, the hydrogen adsorption energies of Ni, around −2.6 eV,[43,44] are much lower than that of Mo in Mo_2C, around −0.8 eV,[45,46] facilitating hydrogen spillover from the NiMo phase to the Mo_2C phase. The Mo_2C lattice, being electron-rich and ordered under cathodic bias, stabilizes and accommodates these H* intermediates, preventing excessive surface coverage on Ni. Electron-rich Mo, with increased d-band occupancy, forms moderate Mo–H bonds that retain H* without hindering its eventual combination into H_2 for hydrogen desorption, thus facilitating the Heyrovsky step. As an example, the hydrogen adsorption strength on Mo_2C was weakened to give a hydrogen adsorption energy of 0.037 eV, close to optimal thermoneutral hydrogen adsorption, upon coupling Mo_2C with Ni that donates electrons to Mo_2C to make Mo electron-rich, with which the HER activity of Mo_2C was much improved.[47] This interfacial synergy ensures efficient coupling of water dissociation and H_2

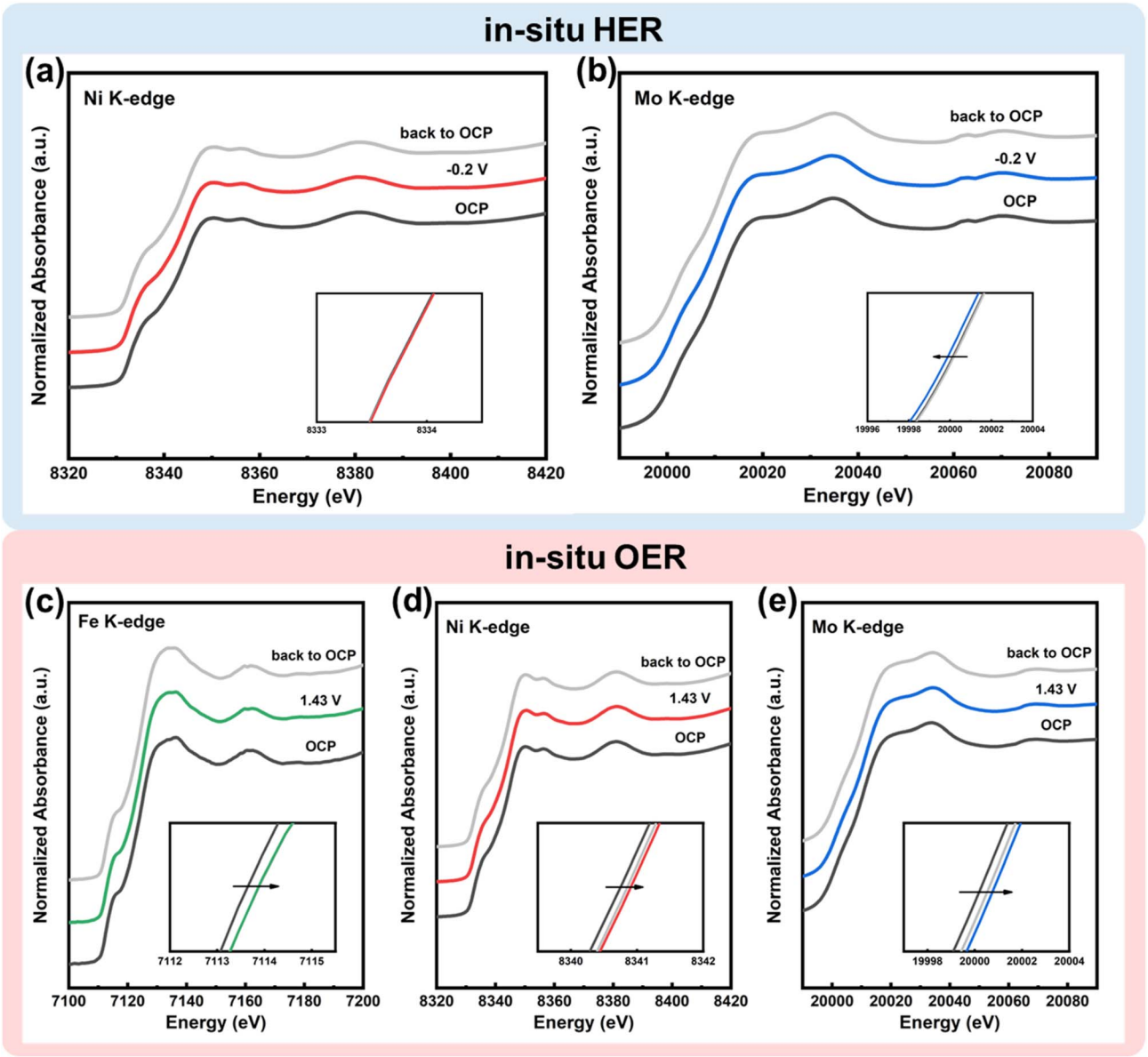

Fig. 6 *In situ* XANES spectra of Mo_2C/NiMo under cathodic conditions at the (a) Ni K-edge and (b) Mo K-edge. *In situ* XANES spectra of Mo_2C/FeNiMo under anodic conditions at the (c) Fe K-edge, (d) Ni K-edge, and (e) Mo K-edge. Cathodic conditions: OCP, −0.20 V, and back to OCP. Anodic conditions: OCP, 1.43 V, and back to OCP. Insets show the corresponding locally enlarged overlaid curves.

desorption during the alkaline HER to realize enhanced HER activities of Mo_2C/NiMo.

Fig. 6c–e show the *in situ* XANES spectra of Fe, Ni, and Mo K-edges of Mo_2C/FeNiMo, respectively under OER conditions. As the applied potential increases from OCP to 1.43 V, the absorption edges of Fe, Ni, and Mo K-edges shift to higher energies, signifying raised valence states of Fe, Ni, and Mo under anodic bias. In alkaline media, the OER proceeds *via* consecutive attack of hydroxide ions on metallic active sites for sequential formation of *OH, *O, and *OOH, followed by desorption of O_2 and recovery of the active sites. The adsorption/formation of these oxygen-containing intermediates leads to electron withdrawal from the metallic sites because of the high electronegativity of oxygen. This results in decreases in electron densities around the metal sites, thereby causing upshifts in valence states and thus absorption edges to higher energies. Fig. S9a–c present the corresponding FT-EXAFS spectra of Fe, Ni, and Mo K-edges. Under OER conditions, the Fe–M and Ni–M coordination intensities drop, which can be attributed to the adsorption/formation of the oxygen-containing intermediates. The adsorption/formation of these oxygen-containing intermediates is dynamic and the structure of the formed oxygen-containing intermediates is amorphous, both leading to increased disorder of the local structure around Fe and Ni and subsequent drops in coordination intensities of the two elements. As for the Mo K-edge spectrum, under OER conditions, the Mo–C coordination shell intensity increases, which can be attributed to partial surface oxidation of Mo_2C,

converting surface Mo–C bonds to Mo–O bonds. The Mo–C bond is less ordered for electron-deficient Mo under anodic potentials (Fig. 6e) as compared with the Mo–O bond, which is ordered in the MoO_x structure. In addition, O is a heavier atom than C, and offers stronger backscattering strength to the Mo–O coordination, which overlaps with the Mo–C coordination. The two factors lead to enhanced Mo–C coordination shell intensity. In the Mo_2C/FeNiMo heterostructured catalyst, electrons flow from the FeNiMo domain to the Mo_2C domain (Fig. 3g), leading to more electropositive Fe and Ni for favorable formation of active high-valent intermediates, *OOH, and consequent enhancements in OER activities.

In situ Raman spectroscopy was conducted to monitor the structural evolution of Mo_2C/NiMo and Mo_2C/FeNiMo under cathodic and anodic potentials, respectively. Fig. S10a shows the *in situ* Raman spectra of Mo_2C/NiMo under HER conditions. Evidently, no significant spectral features emerge during the whole potential course, decreasing from OCP to −0.4 V and back to OCP. In the HER process, no Raman-active intermediates were formed. In contrast, under OER conditions, Mo_2C/FeNiMo exhibits distinct spectral features upon application of increasing potentials from OCP up to 1.63 V, as shown in Fig. S10b. Two broad Raman peaks emerge centered around 480 and 560 cm^{-1}, attributable to formation of (Ni/Fe)*–OOH intermediates.[48] It has been demonstrated with DFT calculations that Fe-doped NiOOH is thermodynamically favorable, with Fe existing in a low spin state.[49] The low spin state of Fe renders the surface Fe sites highly active for OER. The thermodynamic OER overpotentials computed for Fe-doped and pure NiOOH were 0.42 and 0.77 V, respectively, demonstrating Fe-doping induced activity enhancement.[49] These two characteristic Raman peaks first emerge at 1.43 V and continuously intensify with increasing anodic potentials. The formation of (Ni/Fe)–OOH intermediates reveals that Ni and Fe are the active sites for OER catalysis. The Mo_2C in Mo_2C/FeNiMo withdraw electrons from FeNiMo, making Ni and Fe more electropositive for more favorable formation of the active oxyhydroxide intermediates and thus enhanced OER activities (Fig. 4d).

4. Conclusion

In this study, a simple and fast dip–roast–reduction process was successfully developed to uniformly load carbide/alloy heterostructured catalysts onto Ni foam substrates. For HER and OER, Mo_2C/NiMo and Mo_2C/FeNiMo heterostructures were specifically designed, respectively, both exhibiting outstanding electrocatalytic efficiency. For HER, Mo_2C/NiMo required overpotentials of only 37 and 169 mV to reach current densities of 10 and 500 mA cm^{-2}, respectively, with a Tafel slope of 74.6 mV dec^{-1}, suggesting a Volmer–Heyrovsky mechanism. For OER, Mo_2C/FeNiMo achieved low overpotentials of 218 and 303 mV to deliver current densities of 10 and 500 mA cm^{-2}, respectively, with a Tafel slope of only 32.7 mV dec^{-1}, indicating fast OER kinetics. XRD, TEM, and XPS analyses confirmed the heterostructure features of the catalysts, whereas electrochemical measurements confirmed the positive synergy between the carbide and alloy phases for much enhanced activities derived from the heterostructures. When applied in an AEMWE, the MEA constructed with Mo_2C/NiMo@NF//PiperION//Mo_2C/FeNiMo@NF exhibited remarkable water electrolysis performances, delivering an ultrahigh current density of 2.645 A cm^{-2} at 2.0 V. Moreover, a long-term durability test at 0.5 A cm^{-2} over 50 h showed only a 2.0% decay, confirming the excellent chemical and mechanical stability and practical applicability of these catalysts under alkaline conditions. The Mo_2C/NiMo and Mo_2C/FeNiMo heterostructured catalysts, constructed from the combination of carbides and alloys, exhibited excellent catalytic activities by leveraging electronic modulations, optimized adsorption of hydrogen and oxygenated intermediates, and positive synergy between the constituent phases. These results highlight the great potential of carbide/alloy heterostructured catalysts for practical alkaline water electrolysis applications.

Author contributions

Kai-An Lee: writing – original draft, conceptualization, data curation, formal analysis, investigation, methodology, validation, visualization. Yu-Chieh Ting: data curation, formal analysis. Chiung-Wen Chang: data curation, formal analysis. Tzu-Hsiang Lin: data curation, formal analysis. Shao-I. Chang: data curation, formal analysis. Tsung-Wei Hsueh: data curation, formal analysis. Shih-Yuan Lu: writing – review and editing, conceptualization, formal analysis, investigation, methodology, validation, supervision, resources, project administration, funding acquisition.

Conflicts of interest

The authors declare that they have no known competing financial interests or personal relationships that could have appeared to influence the work reported in this paper.

Data availability

The data supporting this article have been included as part of the supplementary information (SI). Supplementary information: Scheme S1, Fig. S1–S7, and Tables S1–S12. See DOI: https://doi.org/10.1039/d6ta02888h.

Acknowledgements

The authors acknowledge the financial support offered by the National Science and Technology Council (NSTC) of Taiwan through grants 113-2218-E-007-013 and 113-2221-E-007-032-MY3. The authors greatly appreciate the beamtime at TPS 44A1 provided by the National Synchrotron Radiation Research Center (NSRRC) of Taiwan, ROC. The authors also acknowledge access to spherical-aberration-corrected transmission electron microscopy (JEM-ARM200FTH, JEOL Ltd) and high-resolution X-ray photoelectron spectroscopy (HR-XPS, PHI Quantera II, ULVAC-PHI Inc.) at the Instrumentation Center of National Tsing Hua University.

References

1 Y. Yan, B. Y. Xia, B. Zhao and X. Wang, A review on noble-metal-free bifunctional heterogeneous catalysts for overall electrochemical water splitting, *J. Mater. Chem. A*, 2016, **4**, 17587–17603.
2 X. Li, X. Hao, A. Abudula and G. Guan, Nanostructured catalysts for electrochemical water splitting: current state and prospects, *J. Mater. Chem. A*, 2016, **4**, 11973–12000.
3 C. Hu, L. Zhang and J. Gong, Recent progress made in the mechanism comprehension and design of electrocatalysts for alkaline water splitting, *Energy Environ. Sci.*, 2019, **12**, 2620–2645.
4 C. Li and J. B. Baek, The promise of hydrogen production from alkaline anion exchange membrane electrolyzers, *Nano Energy*, 2021, **87**, 106162.
5 N. Du, C. Roy, R. Peach, M. Turnbull, S. Thiele and C. Bock, Anion-exchange membrane water electrolyzers, *Chem. Rev.*, 2022, **13**, 11830–11895.
6 Y. Yang, P. Li, X. Zheng, W. Sun, S. X. Dou, T. Ma and H. Pan, Anion-exchange membrane water electrolyzers and fuel cells, *Chem. Soc. Rev.*, 2022, **51**, 9620–9693.
7 I. Vincent and D. Bessarabov, Low cost hydrogen production by anion exchange membrane electrolysis: A review, *Renewable Sustainable Energy Rev.*, 2018, **81**, 1690–1704.
8 L. Wan, Z. Xu, Q. Xu, M. Pang, D. Lin, J. Liu and B. Wang, Key components and design strategy of the membrane electrode assembly for alkaline water electrolysis, *Energy Environ. Sci.*, 2023, **16**, 1384–1430.
9 C.-W. Chang, Y.-C. Ting, K.-A. Lee, S.-I. Chang, K.-H. Lin and S.-Y. Lu, Interface engineering effected charge redistribution within high entropy alloy-metal heterostructured catalyst enables high performance anion exchange membrane water electrolysis, *Small*, 2026, **22**, e10665.
10 F.-Y. Yen, S.-I. Chang, Y.-C. Ting, C.-W. Chang, K.-A. Lee and S.-Y. Lu, In-situ selective oxidation created Cr_2O_3 assisting CrMnFeCoNi for ultrahigh power density zinc–air batteries, *Energy Mater.*, 2025, **5**, 500114.
11 G. Zhao, K. Rui, S. X. Dou and W. Sun, Heterostructures for electrochemical hydrogen evolution reaction: a review, *Adv. Funct. Mater.*, 2018, **28**, 1803291.
12 W. Zhang, L. Yang, Z. Li, G. Nie, X. Cao, Z. Fang, X. Wang, S. Ramakrishna, Y. Long and L. Jiao, Regulating hydrogen/oxygen species adsorption via built-in electric field-driven electron transfer behavior at the heterointerface for efficient water splitting, *Angew. Chem., Int. Ed.*, 2024, **63**, e202400888.
13 J. Wei, M. Zhou, A. Long, Y. Xue, H. Liao, C. Wei and Z. J. Xu, Heterostructured electrocatalysts for hydrogen evolution reaction under alkaline conditions, *Nano-Micro Lett.*, 2018, **10**, 75.
14 P. Chen, J. Ye, H. Wang, L. Ouyang and M. Zhu, Recent progress of transition metal carbides/nitrides for electrocatalytic water splitting, *J. Alloys Compd.*, 2021, **883**, 160833.
15 Y. Zhong, X. Xia, F. Shi, J. Zhan, J. Tu and H. J. Fan, Transition metal carbides and nitrides in energy storage and conversion, *Adv. Sci.*, 2016, **3**, 1500286.
16 T.-H. Lin, Y.-C. Ting, C.-W. Chang, S.-I. Chang, K.-A. Lee, T.-W. Hsueh, K.-H. Lin and S.-Y. Lu, 3-d element induced charge redistribution of bimetallic η-phase carbides leads to high performance electrocatalysts for highly efficient anion exchange membrane water electrolysis, *Small*, 2025, **21**, e11280.
17 J. Diao, Y. Qiu, S. Liu, W. Wang, K. Chen, H. Li, W. Yuan, Y. Qu and X. Guo, Interfacial engineering of W_2N/WC heterostructures derived from solid-state synthesis: a highly efficient trifunctional electrocatalyst for ORR, OER, and HER, *Adv. Mater.*, 2020, **32**, 1905679.
18 Z. Zhao, F. Qin, S. Kasiraju, L. Xie, M. K. Alam, S. Chen, D. Wang, Z. Ren, Z. Wang, L. C. Grabow and J. Bao, Vertically aligned MoS_2/Mo_2C hybrid nanosheets grown on carbon paper for efficient electrocatalytic hydrogen evolution, *ACS Catal.*, 2017, **7**, 7312–7318.
19 Y. Xu, J. Yang, T. Liao, R. Ge, Y. Liu, J. Zhang, Y. Li, M. Zhu, S. Li and W. Li, Bifunctional water splitting enhancement by manipulating Mo-H bonding energy of transition Metal-Mo_2C heterostructure catalysts, *Chem. Eng. J.*, 2022, **431**, 134126.
20 S. Yuan, L. Xiang, N. Li, T. Liang, K. Wang, X. Gao, M. Cui and L. Zhao, Modulating electronic structure and mass transfer kinetics via Mo-Mo_2C heterostructure for ampere-level hydrogen evolution, *Adv. Funct. Mater.*, 2025, **35**, 2422514.
21 A. Jain, S. P. Ong, G. Hautier, W. Chen, W. D. Richards, S. Dacek, S. Cholia, D. Gunter, D. Skinner, G. Ceder and K. A. Persson, Commentary: The Materials Project: A materials genome approach to accelerating materials innovation, *APL Mater.*, 2013, **1**, 011002.
22 F. Silvearv, P. Larsson, S. L. T. Jones, R. Ahuja and J. A. Larsson, Establishing the most favorable metal-carbon bond strength for carbon nanotube catalysts, *J. Mater. Chem. C*, 2015, **3**, 3422–3427.
23 W. Liu, Y. Yang, L. Chen, E. Xu, J. Xu, S. Hong, X. Zhang and M. Wei, Atomically-ordered active sites in NiMo intermetallic compound toward low-pressure hydrodeoxygenation of furfural, *Appl. Catal., B*, 2021, **282**, 119569.
24 C. L. Huang, Y. G. Lin, C.-L. Chiang, C.-K. Peng, D. Senthil Raja, C.-T. Hsieh, Y.-A. Chen and S.-Y. Lu, Atomic scale synergistic interactions lead to breakthrough catalysts for electrocatalytic water splitting, *Appl. Catal., B*, 2023, **320**, 122016.
25 H. Yang, X. Chen, G. Hu, W.-T. Chen, S. J. Bradley, W. Zhang, G. Verma, T. Nann, D.-E. Jiang, P. E. Kruger, X. Wang, H. Tian, G. I. N. Waterhouse, S. G. Telfer and S. Ma, Highly efficient electrocatalytic hydrogen evolution promoted by O–Mo–C interfaces of ultrafine β-Mo_2C nanostructures, *Chem. Sci.*, 2020, **11**, 3523–3530.
26 H. Zhang, H. Jin, Y. Yang, F. Sun, Y. Liu, X. Du, S. Zhang, F. Song, J. Wang, Y. Wang and Z. Jiang, Understanding the synergetic interaction within α-MoC/β-Mo_2C

heterostructured electrocatalyst, *J. Energy Chem.*, 2019, **35**, 66–70.
27 G. Qian, J. Chen, T. Yu, J. Liu, L. Luo and S. Yin, Three-phase heterojunction NiMo-based nano-needle for water splitting at industrial alkaline condition, *Nano-Micro Lett.*, 2022, **14**, 20.
28 Y. Zhang, Y. Wang, S. Jia, H. Xu, J. Zang, J. Lu and X. Xu, A hybrid of NiMo-Mo_2C/C as non-noble metal electrocatalyst for hydrogen evolution reaction in an acidic solution, *Electrochim. Acta*, 2016, **222**, 747–754.
29 Z. Yang, M. Li, S. Chen, S. Yang, F. Peng, J. Liao, Y. Fang, S. Zhang and S. Zhang, Cocatalyst engineering with robust tunable carbon-encapsulated Mo-rich Mo/Mo_2C heterostructure nanoparticle for efficient photocatalytic hydrogen evolution, *Adv. Funct. Mater.*, 2023, **33**, 2212746.
30 F. Attar, A. Riaz, D. Zhang, H. Lu, L. Thomsen and S. Karuturi, Advanced NiMoC electrocatalysts precision synthesised at room temperature for efficient hydrogen evolution across pH ranges, *Chem. Eng. J.*, 2025, **518**, 164494.
31 Y. Zhang, X. Zhen, Z. Su, J. Guo, J. Li, S. Liu and X. Li, Ni/MoC@NC as bifunctional electrocatalyst coupled HER and Urea oxidation for energy-efficient hydrogen production, *Int. J. Hydrogen Energy*, 2024, **60**, 46–54.
32 Z. Xu, S. Jin, M. H. Seo and X. Wang, Hierarchical Ni-Mo_2C/N-doped carbon Mott-Schottky array for water electrolysis, *Appl. Catal., B: Environ. Energy*, 2021, **292**, 120168.
33 L. Ying, S. Sun, W. Liu, H. Zhu, Z. Zhu, A. Liu, L. Yang, S. Lu, F. Duan, C. Yang and M. Du, Heterointerface engineering in bimetal alloy/metal carbide for superior hydrogen evolution reaction, *Renewable Energy*, 2020, **161**, 1036–1045.
34 M. Li, Y. Zhu, H. Wang, C. Wang, N. Pinna and X. Lu, Ni Strongly coupled with Mo_2C encapsulated in nitrogen-doped carbon nanofibers as robust bifunctional catalyst for overall water splitting, *Adv. Energy Mater.*, 2019, **9**, 1803185.
35 J. H. Sun, J. N. Liu, H. Chen, X. Han, Y. Wu, J. He, C. Han, G. Yang and Y. Shan, Strongly coupled Mo_2C and Ni nanoparticles with in-situ formed interfaces encapsulated by porous carbon nanofibers for efficient hydrogen evolution reaction under alkaline conditions, *J. Colloid Interface Sci.*, 2020, **558**, 100–105.
36 F. Chen, M. Tang, J. Zhou, H. Zhang, C. Su and S. Guo, Fe-based amorphous alloy wire as highly efficient and stable electrocatalyst for oxygen evolution reaction of water splitting, *J. Alloys Compd.*, 2023, **955**, 170253.
37 H. Liu, C. Xi, J. H. Xin, G. L. Zhang, S. F. Zhang, Z. J. Zhang, Q. Huang, J. Li, H. Liu and J. Kang, Free-standing nanoporous NiMnFeMo alloy: an efficient non-precious metal electrocatalyst for water splitting, *Chem. Eng. J.*, 2021, **404**, 126530.
38 A. Lasia, Mechanism and kinetics of the hydrogen evolution reaction, *Int. J. Hydrogen Energy*, 2019, **44**, 19484–19518.
39 A. C. Lazanas and M. I. Prodromidis, Electrochemical impedance spectroscopy—a tutorial, *ACS Meas. Sci. Au*, 2023, **3**, 162–193.
40 M. Hou, L. Zheng, D. Zhao, X. Tan, W. Feng, J. Fu, T. Wei, M. Cao, J. Zhang and C. Chen, Microenvironment reconstitution of highly active Ni single atoms on oxygen-incorporated Mo_2C for water splitting, *Nat. Commun.*, 2024, **15**, 1342.
41 C. Lei, Y. Wang, Y. Hou, P. Liu, J. Yang, T. Zhang, X. Zhuang, M. Chen, B. Yang, L. Lei, C. Yuan, M. Qiu and X. Feng, Efficient alkaline hydrogen evolution on atomically dispersed Ni–N_x Species anchored porous carbon with embedded Ni nanoparticles by accelerating water dissociation kinetics, *Energy Environ. Sci.*, 2019, **12**, 149.
42 P. A. Sermon and G. C. Bond, Hydrogen spillover, *Catal. Rev.*, 1974, **8**, 211–239.
43 M. H. Weng, H.-T. Chen, Y.-C. Wang, S.-P. Ju, J.-G. Chang and M.-C. Lin, Kinetics and mechanisms for the adsorption, dissociation, and diffusion of hydrogen in Ni and Ni/YSZ slabs: a DFT study, *Langmuir*, 2012, **28**, 5596–5605.
44 A. Michaelides and P. Hua, A density functional theory study of CH_2 and H adsorption on Ni(111), *J. Chem. Phys.*, 2000, **112**, 6006–6014.
45 S. Posada-Pérez, F. Viñes, R. Valero, J. A. Rodriguez and F. Illas, Adsorption and dissociation of molecular hydrogen on orthorhombic β-Mo_2C and cubic δ-MoC (001) surfaces, *Surf. Sci.*, 2017, **656**, 24–32.
46 A. J. Medford, A. Vojvodic, F. Studt, F. Abild-Pedersen and J. K. Nørskov, Elementary steps of syngas reactions on Mo_2C(001): adsorption thermochemistry and bond dissociation, *J. Catal.*, 2012, **290**, 108–117.
47 Z. Liu, H. He, Y. Liu, Y. Zhang, J. Shi, J. Xiong, S. Zhou, J. Li, L. Fan and W. Cai, Soft-template derived Ni/Mo_2C hetero-sheet arrays for large current density hydrogen evolution reaction, *J. Colloid Interface Sci.*, 2023, **635**, 23–31.
48 Z. Qiu, Y. Ma and T. Edvinsson, In operando Raman investigation of Fe doping influence on catalytic NiO intermediates for enhanced overall water splitting, *Nano Energy*, 2019, **66**, 104118.
49 Z.-D. He, R. Tesch, M. J. Eslamibidgoli, M. H. Eikerling and P. M. Kowalski, Low-spin state of Fe in Fe-doped NiOOH electrocatalysts, *Nat. Commun.*, 2023, **14**, 3498.

